

RaNeuS: Ray-adaptive Neural Surface Reconstruction

Yida Wang¹ David Joseph Tan² Nassir Navab¹ Federico Tombari^{1,2}
¹ Technische Universität München ² Google

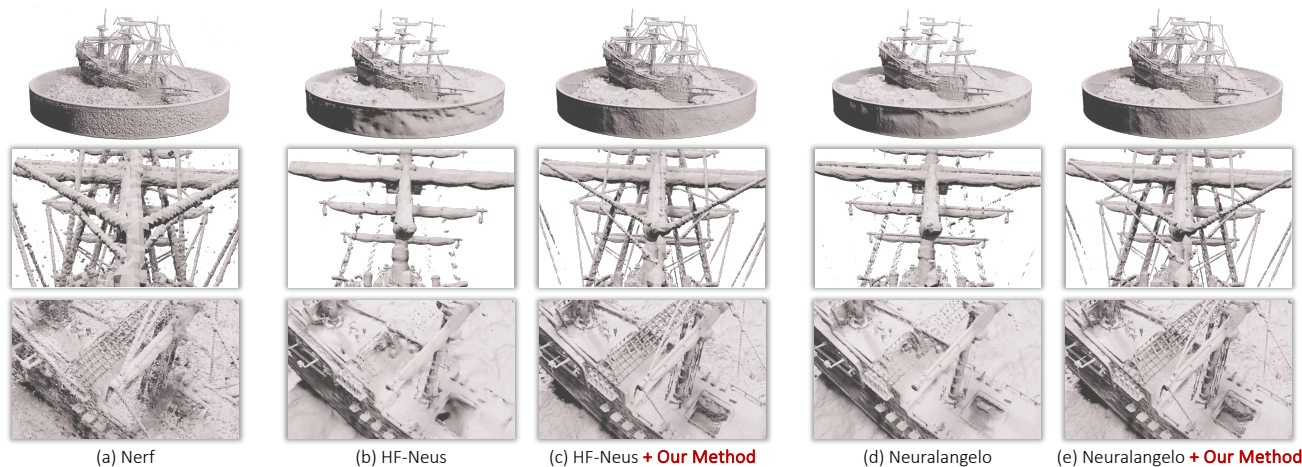


Figure 1. We improve the accuracy of the extracted surfaces \mathbf{S} from signed distance field (SDF) based on follow-up works of NeuS [34], e.g. HF-NeuS [36] in (b) and Neuralangelo [20] in (d). Surfaces of all NeuS variants are extracted from zero-crossing space in SDF $f(\cdot)$, while surfaces of NeRF [25] in (a) are extracted from a learned density field $\sigma(\cdot)$ with a threshold of 15. Our proposed method in (c) and (e) uncovers the lost details in NeuS-based methods with respect to (a), while keeping the smoothness in SDF compared to surfaces extracted from NeRF.

Abstract

Our objective is to leverage a differentiable radiance field e.g. NeRF to reconstruct detailed 3D surfaces in addition to producing the standard novel view renderings. There have been related methods that perform such tasks, usually by utilizing a signed distance field (SDF). However, the state-of-the-art approaches still fail to correctly reconstruct the small-scale details, such as the leaves, ropes, and textile surfaces. Considering that different methods formulate and optimize the projection from SDF to radiance field with a globally constant Eikonal regularization, we improve with a ray-wise weighting factor to prioritize the rendering and zero-crossing surface fitting on top of establishing a perfect SDF. We propose to adaptively adjust the regularization on the signed distance field so that unsatisfying rendering rays won't enforce strong Eikonal regularization which is ineffective, and allow the gradients from regions with well-learned radiance to effectively back-propagated to the SDF. Consequently, balancing the two objectives in order

to generate accurate and detailed surfaces. Additionally, concerning whether there is a geometric bias between the zero-crossing surface in SDF and rendering points in the radiance field, the projection becomes adjustable as well depending on different 3D locations during optimization. Our proposed RaNeuS¹ are extensively evaluated on both synthetic and real datasets, achieving state-of-the-art results on both novel view synthesis and geometric reconstruction.

1. Introduction

Understanding the 3D structure from multi-view stereo (MVS) data performs well on multiple tasks, e.g. dense reconstruction [4, 9, 10, 17], novel-view synthesis [25, 26, 28] and watertight surface reconstruction [34–36, 43]. Limiting the scope to reconstruction, MVS leverages the images collected from different camera positions to build a digi-

¹Codes are released at <https://github.com/wangyida/ra-neus>.

tal replica of a scene or an object. Although traditional MVS reconstruction pipeline, *e.g.* Poisson [17] or Delaunay [4, 10], performs well on both indoor and outdoor scenarios, they still have difficulty in reconstructing the finer details, *i.e.* the surface is too noisy or even incomplete.

More recently, there is a new trend in utilizing neural renderers [25, 26, 28] for reconstruction based on the Neural Radiance Fields (NeRF) [25]. Leveraging the vast information learned in the radiance field, these works [12, 14, 21, 34–36, 43] aim at building the connections between the geometric implicit field, *e.g.* signed distance field (SDF) or unsigned distance field (UDF), to the radiance field. In this way, we can optimize them together so that we can easily extract the mesh directly from learned signed implicit field by matching cube [23] to get watertight meshes.

Determining how to merge the optimizations for novel view synthesis with the optimization for reconstruction is the real challenge. For example, we noticed a race condition in some cases wherein the SDF was optimized faster than the radiance field; consequently, limiting the influence of the radiance field in reconstruction. Therefore, in this work, we focus on capturing the balance between optimizing the appearance and the geometry as shown in Fig. 1 in order to reconstruct fine-grained surfaces of a static scene or an object with the help of neural rendering.

2. Related Works

NeRF [25] and its subsequent works [1, 28, 42] represent a remarkable advancement in novel view synthesis from multi-view stereo images. One disadvantage of training the radiance field is the low training and inference speed. Works introducing coding the input query point in a multi-resolution hash code [26, 35, 43] solves this problem, boosting the research on this topic.

The high-quality novel view rendering indicates a strong prospect for a detailed 3D geometric reconstruction, which is investigated by follow-up works [22, 34, 36]. Common among these methods, the overall framework can be summarized with the three-stage pipeline: (1) camera pose estimation; (2) mesh initialization in signed implicit field; and, (3) efficient mesh refinement. Since the camera poses are usually given, typically computed through COLMAP [30, 31] or HLOC [29], the scope of our paper is associated with a cascaded pipeline with the step (2) to produce a high-quality mesh compared to the related works and then with the step (3) to refine the extracted mesh optimizing for efficiency and the textures on the mesh. In this paper, we observed that the accuracy of the proposed method surpasses the related work even without relying on mesh refinement. The subsequent sections then focus on step (2) involving implicit mesh extraction with learned radiance field in Sec. 2.1 and effective training with hash encoding in Sec. 2.2.

2.1. Neural implicit surface

Extracting the mesh from a signed implicit field $f(\cdot)$, *e.g.* the signed distance field (SDF) [27, 41] or truncated SDF (TSDF) [15], is determined by the values of the sampled positions at a zero threshold. Mathematically, the surface \mathbf{S} of the scene can be obtained by extracting the zero-level set of the SDF. Neural rendering [25] can produce high-quality novel view synthesis, which we can exploit with the help of the learned radiance field. Extracting meshes from the radiance field such as NeuS [34], NeuS2 [35], Instant-NSR [43], and HF-NeuS [36] has shown advantages against constructing meshes using traditional MVS fusion such as MeshMVS [32]. As one of the first few works that extract mesh with the help of radiance field, VolSDF [38] applied the cumulative distribution function of Laplacian distribution to evaluate the density function from SDF for volume rendering and surface reconstruction. NeuralWarp [7] further improved the accuracy on low-textured areas by optimizing consistency between warped views of different images. Another series of works which are variants from NeuS [34], adopted an unbiased density function for signed distance field (SDF) produces more accurate surface reconstruction. One of them is SparseNeuS [22] which extends NeuS to use fewer images for reconstruction. Moreover, HF-NeuS [36] improves NeuS by proposing a simplified unbiased density function, and using hierarchical MLPs for detail reconstruction. Geo-NeuS [8] incorporates structure-from-motion to add more constraints. All of these methods learn SDFs, which can only reconstruct watertight models. In contrast, NeAT [24] represents the 3D surface as a level set of SDF with a validity branch for estimating the surface existence probability at the query positions, which is proven to be helpful to reconstruct mesh for arbitrary topologies such as clothes in D3D [44] dataset.

Presenting the surface in an unsigned distance field [6] (UDF) is another solution to reconstruct arbitrary topologies. MeshUDF [12] is one of the first works proposing to extract mesh from a UDF, which can perform better in reconstructing non-watertight surfaces. More recently, learning UDF with the help of the radiance field is also practical, as long as the parameterized UDF is differentiable. NeuralUDF [21] is used to learn in reconstructing 3D surfaces with arbitrary topologies. It adapts the density function of NeuS to UDFs by introducing an indicator function. However, this method can only learn highly-textured models due to the complex density function used in training. In contrast, NeUDF [14] proposes a UDF training method capable of reconstructing highly textured and textureless models without requiring masks. However, the problem of NeUDF is the biased rendering density field conditioned on the object surface.

2.2. Hash encoding

To solve the training efficiency issue in neural rendering, Instant-NGP [26] proposes to use a hash encoding. Such an idea of encoding the input 3D positions $x \in \mathbb{R}^3$ into hash code using MLP for neural rendering generates an obvious advantage in converging speed compared to NeRF [25] and NeuS [34]. But the meshes extracted from Instant-NGP do not reach the quality of neural rendering methods embedded with an implicit field as the intermediate feature space [34, 36, 43] in terms of surface mesh reconstruction smoothness and precision. This is mainly because of the unknown threshold in extracting the surface mesh with a marching cube. More recently, NeuS 2 [35], Instant-NSR [43], and Neuralangelo [20] were proposed to utilize multi-resolution 3D hash grids and neural surface rendering to achieve superior results in recovering dense 3D surface structures from multi-view images, enabling highly detailed large-scale scene reconstruction from RGB video captures.

3. Methodology

Given a set of calibrated multi-view images capturing an object or a static scene with their corresponding camera poses, we jointly learn a structural surface \mathbf{S} and the appearance \mathbf{C} of the targeted scene through the appearance supervision [21, 34, 36]. The learned set $\{\mathbf{S}, \mathbf{C}\}$ are represented from the signed distance field (SDF) $f(x) : \mathbb{R}^3 \rightarrow \mathbb{R}$ where the value of each element is determined by a 3D position x , and a radiance field $c(x, v) : \mathbb{R}^3 \times \mathbb{S}^2 \rightarrow \mathbb{R}^3$ which is determined by both the position x and the viewing direction $v \in \mathbb{S}^2$. Aiming at learning more precise zero-crossing surfaces in SDF by jointly training the SDF and the radiance field, we introduce two proposed factors λ_r and λ_r to make the SDF regularization more adaptive to improve the rendering quality and reduce the geometric bias.

3.1. Neural rendering

By enforcing the radiance supervision through the 2D image, NeRF [25] leverages volume rendering to match the ground truth for every camera pose with the rendered image. Specifically, we can generate the RGB for every pixel of an image by sampling n points $\{r(t_i) = o + t_i \cdot v \mid i = 1, \dots, n\}$ along its camera ray r , where o is the center of the camera, t_i is the sampling interval along the ray and v is the view direction. By accumulating the radiance field density $\sigma(r(t))$ and colors $c(r(t), v)$ of the sample points, we can compute the color $\hat{\mathbf{C}}$ of the ray as

$$\hat{\mathbf{C}}(r) = \int_{t_n}^{t_f} T(t) \cdot \sigma(r(t)) \cdot c(r(t), v) dt \quad (1)$$

where the transparency $T(t)$ is derived from the volume density $\sigma(r(t))$. $T(t)$ denotes the accumulated transmittance along the ray r from the closest point t_n to the farthest

point t_f such that

$$T(t) = \exp\left(-\int_{t_n}^t \sigma(r(s)) ds\right). \quad (2)$$

Note that $T(t)$ is a monotonic decreasing function with a starting value $T(t_n)$ of 1. The product $T(t) \cdot \sigma(r(t))$ is used as a weight $\omega(t)$ in the volume rendering of radiance in (1).

Since the rendering process is differentiable, our model can then learn the radiance field c from the multi-view images with the loss function that minimizes the color difference between the rendered pixels $\hat{\mathbf{C}}(r)$ with $i \in \{1, \dots, m\}$ and the corresponding ground truth pixels $\mathbf{C}(r)$ without 3D supervision as

$$\mathcal{L}_{\text{rgb}} = \frac{1}{m} \sum_{i=1}^m \left(\|\hat{\mathbf{C}}(r) - \mathbf{C}(r)\|_2 + |\hat{\mathbf{C}}(r) - \mathbf{C}(r)| \right) \quad (3)$$

where m denotes the batch size during training. Based on the same input and output, we would further investigate a way to implicitly learn a signed distance field f to extract meshes embedded in (1) during training.

3.2. Ray-adaptive SDF optimization

Aiming at extracting a 3D mesh from a region of interest in the neural rendering, it is plausible to get a projection from a signed distance function (SDF) to the radiance field. Here, we look for a function Φ that transforms the signed distance function so that it can be used to compute the density-related term $T(t)\sigma(r(t))$ in (1).

We build our solution on top of HF-NeuS [36], where they set $\Phi(r(t))$ as the transparency $T(t)$. Notably, the derivative of the transparency function $T(t)$ is the negative weighting function as

$$\frac{d(T(t))}{dt} = -T(t)\sigma(r(t)). \quad (4)$$

Given such formulation, the SDF surface lies on the maximum radiance weight. The maxima is computed by setting the derivative of the weighting function to zero; thus,

$$\frac{d(T(t)\sigma(r(t)))}{dt} = -\frac{d^2(T(t))}{dt^2} = -\frac{d(T'(t))}{dt} = 0. \quad (5)$$

To fulfill the criteria from (4) and (5), HF-NeuS [36] defined the transparency function $T_s(t)$ as the normalized sigmoid function $[1 + \exp(s \cdot f(r(t)))]^{-1}$ with a trainable parameter s . The scalar s reveals how strong the SDF is related to the radiance field, which is usually increasing during training. In the initial stage of training, a small s relaxes the connection between SDF and radiance such that the radiance parametric model is optimized without a dependency on the correct SDF.

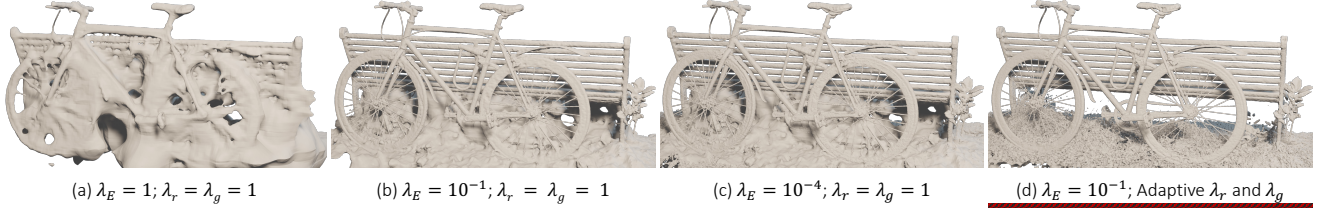


Figure 2. Comparison of the Eikonal regularizer with adaptive factor λ_r and λ_g against constant Eikonal regularizer’s weights on unbounded scene reconstruction in Mip-NeRF 360 dataset [2].

SDF regularization. A signed distance function $f(x)$ is differentiable almost everywhere, while its gradient $\nabla f(x)$ satisfies the Eikonal equation $\|\nabla f(x)\|_2 = 1$. This implies that an SDF can be trained with the Eikonal regularization. According to IGR [11], we enforce an Eikonal loss as a regularizer to make an implicit field act as a signed distance field. However, we discovered that training with a fixed Eikonal regularization [34, 36, 43] can lead to a sub-optimal convergence where the SDF has converged based on the Eikonal regularization but the rendering can still be further optimized. Such a problem harms the improvement of the RGB rendering because the weights are projected from a wrong SDF value, which makes the extracted mesh miss the detailed structures.

Adaptive regularization for rendering. To solve the problem of the reconstruction failures on the thin structures, we found that the capability of rendering such structures from the radiance field should be ensured even when the SDF does not contain the accorded structures so that the gradient could be back-propagated from the radiance field to the SDF later on. Based on the overall loss function $\mathcal{L}_{\text{total}} = \mathcal{L}_{\text{rgb}} + \mathcal{L}_{\text{sdf}}$, we propose to adaptively weight the Eikonal regularization to optimize the SDF as

$$\mathcal{L}_{\text{sdf}} = \frac{\lambda_E}{mn} \sum_{i=1}^m \lambda_r(r_i) \sum_{j=1}^n (\|\mathbf{n}_{ij}\|_2 - 1)^2, \quad (6)$$

where a ray-wise weight $\lambda_r(r_i)$ for the i -th ray r_i is set to be

$$\lambda_r(r_i) = \frac{\alpha}{d_r(r_i) + \alpha}, \quad (7)$$

where $d_r(r_i)$ is the radiance distance $\|\hat{\mathbf{C}}(r_i) - \mathbf{C}(r_i)\|_2$ regarding ray r_i , and α is a positive hyperparameter that is set to be smaller than 1, e.g. $1 \cdot 10^{-6}$. Consequently, the Eikonal regularization will be relaxed when the rendering quality determined by the metric of $d_r(r_i)$ is unsatisfying. In our implementation, the approximated normal $\mathbf{n} = \nabla f(r(\cdot))$ is the derivative of $f(r(\cdot))$, and λ_E is typically set to be 0.1 as mentioned by IGR [11] and NeuS [34].

To avoid extreme values with respect to different scenes, $d_r(r)$ is bounded to a range $[c_{\min}, c_{\max}]$. Notice that we

end up with the typical Eikonal regularization proposed in IGR [11] when we achieve satisfactory renderings measured by the small $d_r(r)$. Thus, in contrast to [11], our approach is more adaptive to the changes in both the rendering and SDF optimizations; thus, relaxing the restrictions from the predefined parameters.

The proposed adaptive Eikonal regularization solves the problem in reconstructing detailed structures through the SDF like the wheel spokes of the bicycle, for which a strong Eikonal constraint will make them disappear as shown in Fig. 2 (a). In contrast, our method was able to capture such structures in Fig. 2 (d). Overall, Fig. 2 illustrates that optimizing with the adaptive Eikonal loss has a better reconstruction of the circular shape of the wheels, the separation between the bench and the grass, and the holes between the blocks of wood on the bench.

Adaptive regularization to reduce geometric bias.

Considering that a simple change in (6) triggered a significant impact on the results. We propose to apply similar relaxing terms for the Eikonal regularization on each sampled point of the selected rays during training. Ideally, the space behind the observed geometric surface contributes far fewer points compared to the empty space in the neural rendering. Although this is a good phenomenon for efficient rendering, it also leads to a problem where an integral rendering point which could serve as an estimated depth point for each ray is biased by the ray’s zero-crossing. As mentioned by D-NeuS [5], the ideal SDF distribution is not guaranteed by the parametric geometric model. Although the parameters of the geometric model are explicitly initialized to produce a spherical SDF, the radiance-based supervision imposes no explicit regularization on the underlying SDF field. The inconsistency between the radiance field and SDF leads to the difficulty of optimizing the inner space in SDF, especially within tiny structures with a small negative space.

Considering D-NeuS defines a weighted rendering point $r(t_r)$ which is $o + t_r \cdot v$ via discretizing and integrating the volume between t_n and t_f as t_r . Referring to the radiance $\hat{\mathbf{C}}(r)$ in (1) of ray r and the transmittance representation $T_s(t)$, our rendering point t_r is weighted summed through

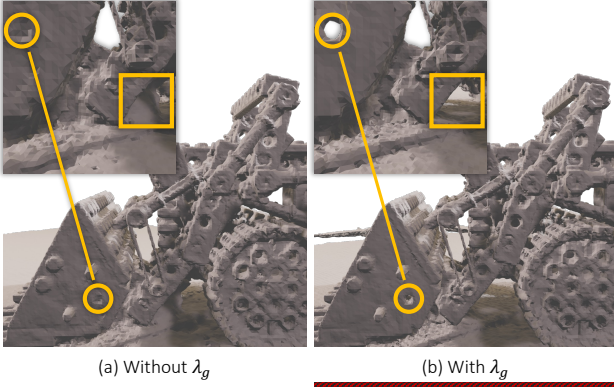


Figure 3. Comparison of Neuralangelo trained with and without the proposed geometric bias factor λ_g on top of the model trained with λ_r .

$\omega(t)$ written as

$$t_r = \frac{\sum_{j=1}^N \omega(t_j) \cdot t_j}{\sum_{j=1}^N \omega(t_j)}, \quad (8)$$

where the weight is represented as

$$\omega(t_j) = \frac{\sigma(r(t_j))}{1 + \exp(s \cdot f(r(t_j)))}. \quad (9)$$

Given the calculated rendering point t_r , we introduce a geometric bias factor λ_g which is

$$\lambda_g = 1 - \frac{t_r - t_s}{t_f - t_n}, \quad (10)$$

where $r(t_s)$ is the approximated zero-crossing by assessing the SDF values along ray $r(\cdot)$. So, in this case, the Eikonal regularization will only be fully enforced when there is no geometric bias between the zero-crossing surface of the SDF and the rendering point in the radiance field. Weighted by $\lambda_g(r)$, the SDF loss also back-propagates gradients to the factor s used in $T_s(t)$ which adjusts the projection from the SDF to the radiance field. Eventually, our final geometric loss is defined as

$$\mathcal{L}_{\text{sdf}} = \frac{\lambda_E}{mn} \sum_{i=1}^m \lambda_g(r_i) \lambda_r(r_i) \sum_{j=1}^n (\|n_{ij}\|_2 - 1)^2. \quad (11)$$

As shown in Fig. 3, our model trained with the additional geometric bias factor $\lambda_g(r)$ successfully reveals the tiny hole in the lifter of the Lego bulldozer in Mip-NeRF 360 [2] dataset.

3.3. Training

Our model is trained to simultaneously run the geometric optimization in 3D space and appearance optimization in

2D space with $\mathcal{L}_{\text{total}}$. The Adam optimizer [18] is adopted with an exponentially decaying learning rate schedule ranging from $1 \cdot 10^{-2}$ to $1 \cdot 10^{-4}$.

Trained with the proposed weighting factors λ_r and λ_g where α is set to be $1 \cdot 10^{-6}$ in (7), a generalizable model *RaNeuS* can be built on top of NeuS 2 [35] with a customized background model. Given x , a hash encoding is obtained at each level $h_i(x) \in \mathbb{R}^d$, where d is the dimension of a feature vector and $i = 1, \dots, L$. The hash codes $h_i(x)$ are presented by interpolating the feature vectors assigned at the surrounding voxel grids at level i . Consequently, the hash encodings at all L levels are then concatenated into the multi-resolution hash encoding $h(x) = \{h_i(x)\}_{i=1}^L \in \mathbb{R}^{L \times d}$. Our base resolution in the hash table is set to be $32 \times 32 \times 32$ and eventually reaches a resolution of $2048 \times 2048 \times 2048$ on the 16th level. Progressive training is applied to stabilize the low-level hash table during training, where the first 4 levels are optimized together in the first 2,000 steps and a new higher level is included for optimization every other 2,000 steps.

To deploy *RaNeuS* in unbounded scenes, we represent the foreground and background space in two separate models. The foreground space is modeled by NeuS 2 in a cubic bounding box which covers the scene at close proximity; while, the background is modeled by a vanilla NeRF for rendering alone which is encoded by MLP without an SDF intermediate, which is learned in a contracted spherical space with a radius of twice the diagonal length of the cuboid.

4. Experiments

Since the proposed approach can be adapted to the existing methods, we demonstrate the advantage of our contributions by integrating them with NeuS 2 [35], HF-NeuS [36] and the more recent Neuralangelo [20]. Both works can benefit from the proposed ray-adaptive factors λ_r and λ_g . We conduct our evaluation on three datasets: Mip-NeRF [1], NeRF-synthetic [25] and DTU [16]. To evaluate the quality of the reconstruction, Chamfer distance is used for 3D geometric evaluation, and PSNR is used for rendering validation.

4.1. Mip-NeRF 360

The Mip-NeRF 360 dataset [2] provides nine unbounded scenes, which include five outdoor and four indoor scenes, each containing a complex central object or area and a detailed background. They relied on COLMAP to estimate the camera poses while the camera intrinsics are shared among all images in a scene. The color harmonization issue is limited here, where the captured outdoor scene is collected when the sky is overcast, ensuring that the camera operator casts soft shadows that minimally affect the illumination in the scene. For the indoor scenes, they relied on large diffuse

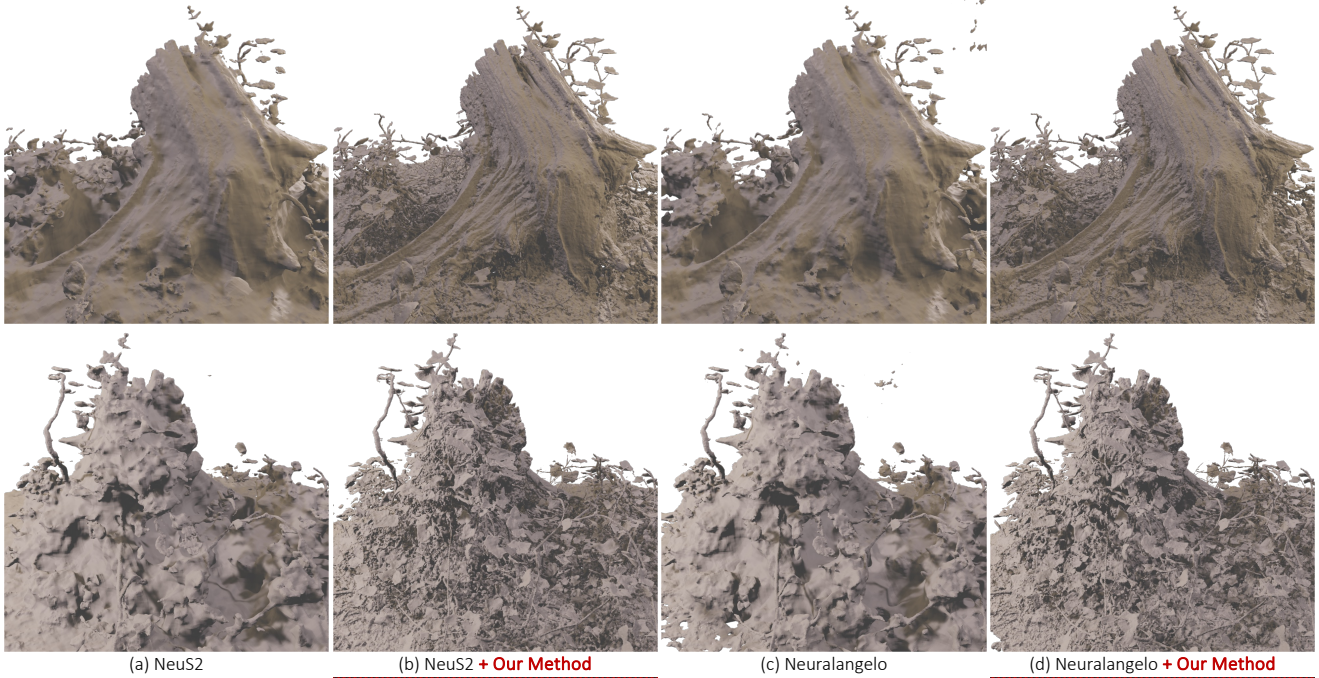


Figure 4. Geometric reconstruction comparison evaluated on the Mip-NeRF 360 dataset [2].

Methods	bicycle	flowers	garden	stump	treehill	room	counter	kitchen	bonsai	Avg.
NeRF [25]	21.76	19.40	23.11	21.73	21.28	28.56	25.67	26.31	26.81	23.85
Mip-NeRF [1]	21.69	19.31	23.16	23.10	21.21	28.73	25.59	26.47	27.13	24.04
NeRF++ [42]	22.64	20.31	24.32	24.34	22.20	28.87	26.38	27.80	29.15	25.11
Deep Blending [13]	21.09	18.13	23.61	24.08	20.80	27.20	26.28	25.02	27.08	23.70
Point-Based [19]	21.64	19.28	22.50	23.90	20.98	26.99	25.23	24.47	28.42	23.71
Mip-NeRF 360 [2]	24.37	21.73	26.98	26.40	22.87	31.63	29.55	32.23	33.46	27.69
NeRF2Mesh [33]	22.44	–	23.13	23.53	–	28.19	24.11	23.75	24.34	–
HF-NeuS [36]	23.99	21.16	26.19	25.26	21.50	30.07	29.14	29.70	34.08	26.78
+ Proposed Method	25.40	22.92	27.65	26.63	23.20	31.80	30.53	31.29	35.75	28.35

Table 1. Mean PSNR on different scenes in Mip-NeRF 360 dataset [2]. HF-NeuS [36] is also parameterized with a background NeRF [25] model for rendering alone to cover the whole unbounded scene.

Methods	bicycle	flowers	garden	stump	treehill	room	counter	kitchen	bonsai	Avg.
NeRF [25]	0.455	0.376	0.546	0.453	0.459	0.843	0.775	0.749	0.792	0.605
Mip-NeRF [1]	0.454	0.373	0.543	0.517	0.466	0.851	0.779	0.745	0.818	0.616
NeRF++ [42]	0.526	0.453	0.635	0.594	0.530	0.852	0.802	0.816	0.876	0.676
Deep Blending [13]	0.466	0.320	0.675	0.634	0.523	0.868	0.856	0.768	0.883	0.666
Point-Based [19]	0.608	0.487	0.735	0.651	0.579	0.887	0.868	0.876	0.919	0.734
Mip-NeRF 360 [2]	0.685	0.583	0.813	0.744	0.632	0.913	0.894	0.920	0.941	0.792
HF-NeuS [36]	0.512	0.547	0.747	0.651	0.585	0.739	0.855	0.726	0.824	0.687
+ Proposed Method	0.721	0.641	0.870	0.797	0.688	0.942	0.926	0.955	0.951	0.832

Table 2. Structural similarity index measure (SSIM) [3, 37] on different scenes in Mip-NeRF 360 dataset [2].

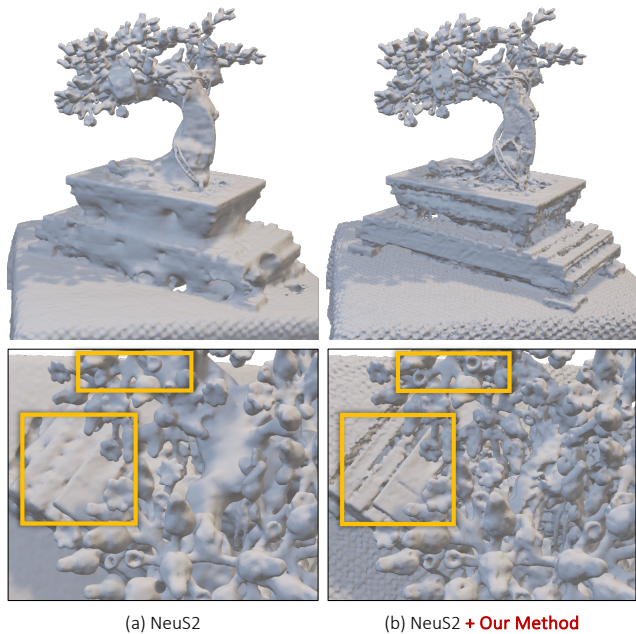


Figure 5. Comparison of our mesh to NeuS 2 [35], focusing on some important details on the bonsai dataset that our method was able to reconstruct while NeuS 2 missed.

Methods	Chair	Ficus	Lego	Mat.	Mic	Ship	Avg.
NeRF [25]	33.00	30.15	32.54	29.62	32.91	28.34	31.09
Mip-NeRF [1]	37.14	33.18	35.74	32.56	38.04	33.08	34.96
VolSDF [38]	25.91	24.41	26.99	28.83	29.46	25.65	26.86
NeuS [34]	27.95	25.79	29.85	29.36	29.89	25.46	28.05
Instant-NSR [43]	34.04	32.47	33.78	27.67	33.43	29.50	31.81
HF-NeuS [36]	28.69	26.46	30.72	29.87	30.35	25.87	28.66
+ Proposed Method	35.26	34.02	34.51	28.99	35.51	33.02	33.55

Table 3. Mean PSNR on different scenes in NeRF-synthetic dataset [25]. Note that the upper parts in this table are methods focusing on rendering alone, while the lower parts in this table contain geometric regularization during training.

light sources. Each scene has between 100 to 330 images with a resolution of 1.0–1.6 megapixels.

We compare the rendering performance with PSNR in Table 1 and SSIM in Table 2. Our model achieves the best overall results of 28.35 for PSNR and 0.832 for SSIM, while Mip-NeRF 360 [2] performs better in a few categories.

In terms of geometry, we highlight in Fig. 5 the amount of detail our results can handle compared to NeuS 2 [35]. Particularly, the over-smoothed NeuS 2 reconstruction of the bonsai is because of the shadows and changes in exposures. The improvement demonstrates that our contributions help overcome this problem. We also include more results against the NeuS 2 [35] and Neuralangelo [20] in Fig. 4 where we illustrate the advantage of the proposed method to reconstruct the finer details.

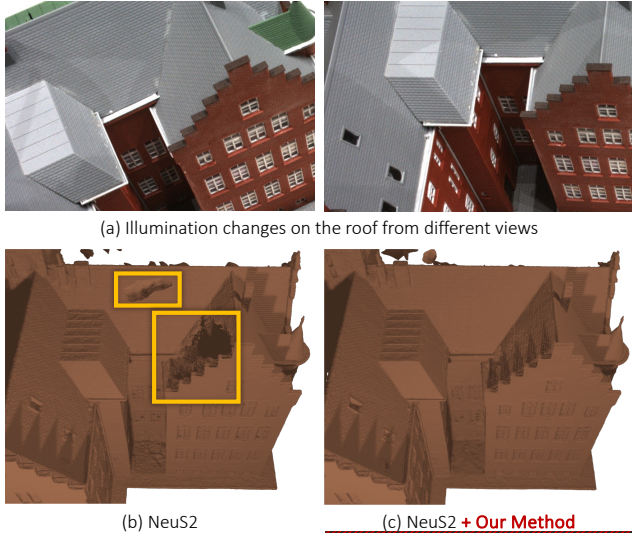


Figure 6. Our adaptive training makes the learned geometry robust against the shadows triggered by the movement of the light source.

4.2. NeRF-synthetic

NeRF-synthetic dataset [25] contains objects with fine-grained detailed and sharp features, such as the Lego bulldozer and a model ship. This dataset was first validated by NeRF [25] for volume rendering. Since it consists entirely of synthetic objects in front of a white background, the rendering task is easier compared to unbounded scenes such as Mip-NeRF 360 dataset [2].

We first compare against NeRF [25] and Mip-NeRF [1] in Table 3 which are methods that focus on novel view synthesis and do not necessarily extract any mesh. Although the proposed method is not the state-of-the-art compared to Mip-NeRF, the gap is noticeably small. Among methods that jointly optimize for geometry and appearance, we demonstrate improved rendering accuracy compared to other methods, achieving the best results. To highlight the improved geometries, we present the qualitative results in Fig. 1, the ropes connecting the poles and the decker are more complete compared to HF-NeuS [36] and Neuralangelo [20].

Considering that NeRF-synthetic is a comparably small dataset, convergence is easily achieved. For this evaluation, all models are coded with hash coding to converge within 20 minutes.

4.3. DTU

DTU [16] is a multi-view stereo dataset. We selected the same 15 models for comparison as the previous methods. Each scene consists of 49 or 64 views with 1600×1200 resolution. As previously mentioned, we use Chamfer distance to measure the accuracy and completeness.

Methods	24	37	40	55	63	65	69	83	97	105	106	110	114	118	122	Avg.
NeRF [25]	26.24	25.74	26.79	27.57	31.96	31.50	29.58	32.78	28.35	32.08	33.49	31.54	31.00	35.59	35.51	30.65
VolSDF [38]	26.28	25.61	26.55	26.76	31.57	31.50	29.38	33.23	28.03	32.13	33.16	31.49	30.33	34.90	34.75	30.38
NeuS [34]	28.20	27.10	28.13	28.80	32.05	33.75	30.96	34.47	29.57	32.98	35.07	32.74	31.69	36.97	37.07	31.97
D-NeuS [5]	28.98	27.58	28.40	28.87	33.71	33.94	30.94	34.08	30.75	33.73	34.84	32.41	31.42	36.76	37.17	32.22
HF-NeuS [36]	29.15	27.33	28.37	28.88	32.89	33.84	31.17	34.83	30.06	33.37	35.44	33.09	32.12	37.13	37.32	32.33
+ Proposed Method	31.14	28.19	29.13	30.09	34.77	35.62	33.84	36.70	33.19	36.44	37.22	35.91	34.55	38.83	39.35	34.33
- without λ_g	31.09	28.21	28.97	29.91	34.25	35.15	33.26	36.74	32.30	36.02	36.96	35.22	34.70	38.29	38.93	34.00
- without λ_r	30.01	28.03	28.41	28.97	33.12	34.15	32.28	35.21	30.94	34.55	35.91	34.22	33.49	37.82	38.29	33.03
Neuralangelo [20]	30.64	27.78	32.70	34.18	35.15	35.89	31.47	36.82	30.13	35.92	36.61	32.60	31.20	38.41	38.05	33.84
+ Proposed Method	32.31	29.71	35.11	35.96	37.57	37.71	33.37	38.35	32.14	38.10	38.90	33.93	33.41	40.24	39.60	35.76
- without λ_g	32.15	29.25	34.72	36.21	37.41	37.21	33.6	38.24	31.59	37.51	38.44	34.13	32.65	40.60	39.37	35.54
- without λ_r	31.65	29.02	34.14	35.24	36.59	37.08	32.4	37.73	31.14	37.10	37.89	33.27	32.67	39.44	38.74	34.94

Table 4. Mean PSNR on different objects in DTU dataset [16].

Methods	24	37	40	55	63	65	69	83	97	105	106	110	114	118	122	Avg.
COLMAP [31]	0.81	2.05	0.73	1.22	1.79	1.58	1.02	3.05	1.40	2.05	1.00	1.32	0.49	0.78	1.17	1.36
Instant-NGP [26]	1.68	1.93	1.57	1.16	2.00	1.56	1.81	2.33	2.16	1.88	1.76	2.32	1.86	1.80	1.72	1.84
IDR [39]	1.63	1.87	0.63	0.48	1.04	0.79	0.77	1.33	1.16	0.76	0.67	0.90	0.42	0.51	0.53	0.90
MVSDF [41]	0.83	1.76	0.88	0.44	1.11	0.90	0.75	1.26	1.02	1.35	0.87	0.84	0.34	0.47	0.46	0.88
RegSDF [40]	0.60	1.41	0.64	0.43	1.34	0.62	0.60	0.90	0.92	1.02	0.60	0.60	0.30	0.41	0.39	0.72
NeRF [25]	1.90	1.60	1.85	0.58	2.28	1.27	1.47	1.67	2.05	1.07	0.88	2.53	1.06	1.15	0.96	1.49
VolSDF [38]	1.14	1.26	0.81	0.49	1.25	0.70	0.72	1.29	1.18	0.70	0.66	1.08	0.42	0.61	0.55	0.86
NeuS [34]	1.00	1.37	0.93	0.43	1.10	0.65	0.57	1.48	1.09	0.83	0.52	1.20	0.35	0.49	0.54	0.84
NeuralWarp [7]	0.49	0.71	0.38	0.38	0.79	0.81	0.82	1.20	1.06	0.68	0.66	0.74	0.41	0.63	0.51	0.68
D-NeuS [5]	0.44	0.79	0.35	0.39	0.88	0.58	0.55	1.35	0.91	0.76	0.40	0.72	0.31	0.39	0.39	0.61
HF-NeuS [36]	0.76	1.32	0.70	0.39	1.06	0.63	0.63	1.15	1.12	0.80	0.52	1.22	0.33	0.49	0.50	0.77
+ Proposed Method	0.50	0.81	0.26	0.26	0.75	0.53	0.54	0.93	0.79	0.64	0.41	0.62	0.30	0.35	0.24	0.53
- without λ_g	0.51	0.82	0.36	0.34	0.81	0.55	0.56	0.98	0.87	0.66	0.43	0.71	0.31	0.40	0.34	0.58
- without λ_r	0.68	1.15	0.58	0.37	0.92	0.59	0.64	1.06	0.99	0.75	0.46	0.93	0.33	0.45	0.41	0.69
Neuralangelo [20]	0.37	0.72	0.35	0.35	0.87	0.54	0.53	1.29	0.97	0.73	0.47	0.74	0.32	0.41	0.43	0.61
+ Proposed Method	0.33	0.65	0.33	0.32	0.90	0.44	0.46	1.32	0.90	0.60	0.40	0.67	0.27	0.29	0.36	0.55
- without λ_g	0.35	0.67	0.33	0.32	0.88	0.49	0.48	1.31	0.90	0.68	0.41	0.68	0.34	0.37	0.39	0.57
- without λ_r	0.37	0.72	0.33	0.36	0.91	0.51	0.52	1.35	0.93	0.69	0.45	0.70	0.36	0.38	0.42	0.60
NeuS 2 [35]	0.56	0.76	0.49	0.37	0.92	0.71	0.76	1.22	1.08	0.63	0.59	0.89	0.40	0.48	0.55	0.70
+ Proposed Method	0.31	0.59	0.29	0.28	0.74	0.45	0.51	1.01	0.82	0.59	0.41	0.73	0.39	0.28	0.29	0.51

Table 5. Fidelity which is reported using Chamfer distance (mm) on different objects in the DTU dataset [16].

Similar to the previous works, we clean the extracted meshes with the object masks dilated by 50 pixels. By doing so, we have achieved better results for both rendering PSNR and mesh reconstruction without using any 3D supervision, such as sparse or dense depth. On average, we reached the state-of-the-art in Table 4 and Table 5. Note that our approach even outperforms RegSDF [40] which was trained with 3D supervision.

Ablation study. In these tables, we included an ablation study to highlight the advantage of each contribution on HF-NeuS and Neuralangelo. Table 4 and Table 5 show that both contributions increase PSNR and reduce the Chamfer distance. Our method shows more robustness against the illumination change among different views as shown in Fig. 6.

5. Conclusion

We propose reconstructing a mesh of a static scene or an object trained with the novel adaptive Eikonal regularization. Compared to the related works, the evaluations on the synthetic and real datasets prove that our model performs the best on novel view synthesis among neural renderers, with implicit fields as intermediate representations. In terms of the 3D reconstruction, our evaluation on the DTU dataset shows that the proposed method has the best and second-best geometric reconstruction accuracy. The thin structures in training images are utilized precisely as visual cues to optimize the SDF in 3D space.

References

- [1] Jonathan T Barron, Ben Mildenhall, Matthew Tancik, Peter Hedman, Ricardo Martin-Brualla, and Pratul P Srinivasan. 2021. Mip-nerf: A multiscale representation for anti-aliasing neural radiance fields. In *Proceedings of the IEEE/CVF International Conference on Computer Vision*. 5855–5864. [2](#), [5](#), [6](#), [7](#)
- [2] Jonathan T Barron, Ben Mildenhall, Dor Verbin, Pratul P Srinivasan, and Peter Hedman. 2022. Mip-nerf 360: Unbounded anti-aliased neural radiance fields. In *Proceedings of the IEEE/CVF Conference on Computer Vision and Pattern Recognition*. 5470–5479. [4](#), [5](#), [6](#), [7](#)
- [3] Dominique Brunet, Edward R Vrscay, and Zhou Wang. 2011. On the mathematical properties of the structural similarity index. *IEEE Transactions on Image Processing* 21, 4 (2011), 1488–1499. [6](#)
- [4] Frédéric Cazals and Joachim Giesen. 2006. Delaunay triangulation based surface reconstruction. In *Effective computational geometry for curves and surfaces*. Springer, 231–276. [1](#), [2](#)
- [5] Decai Chen, Peng Zhang, Ingo Feldmann, Oliver Schreer, and Peter Eisert. 2023. Recovering Fine Details for Neural Implicit Surface Reconstruction. In *Proceedings of the IEEE/CVF Winter Conference on Applications of Computer Vision*. 4330–4339. [4](#), [8](#)
- [6] Julian Chibane, Gerard Pons-Moll, et al. 2020. Neural unsigned distance fields for implicit function learning. *Advances in Neural Information Processing Systems* 33 (2020), 21638–21652. [2](#)
- [7] François Darmon, Bénédicte Bascle, Jean-Clément Devaux, Pascal Monasse, and Mathieu Aubry. 2022. Improving neural implicit surfaces geometry with patch warping. In *Proceedings of the IEEE/CVF Conference on Computer Vision and Pattern Recognition*. 6260–6269. [2](#), [8](#)
- [8] Qiancheng Fu, Qingshan Xu, Yew Soon Ong, and Wenbing Tao. 2022. Geo-neus: Geometry-consistent neural implicit surfaces learning for multi-view reconstruction. *Advances in Neural Information Processing Systems* 35 (2022), 3403–3416. [2](#)
- [9] Yasutaka Furukawa and Jean Ponce. 2009. Accurate, dense, and robust multiview stereopsis. *IEEE transactions on pattern analysis and machine intelligence* 32, 8 (2009), 1362–1376. [1](#)
- [10] Meenakshisundaram Gopi, Shankar Krishnan, and Cláudio T Silva. 2000. Surface reconstruction based on lower dimensional localized Delaunay triangulation. In *Computer Graphics Forum*, Vol. 19. Wiley Online Library, 467–478. [1](#), [2](#)
- [11] Amos Gropp, Lior Yariv, Niv Haim, Matan Atzmon, and Yaron Lipman. 2020. Implicit geometric regularization for learning shapes. *arXiv preprint arXiv:2002.10099* (2020). [4](#)
- [12] Benoit Guillard, Federico Stella, and Pascal Fua. 2022. Meshudf: Fast and differentiable meshing of unsigned distance field networks. In *Computer Vision–ECCV 2022: 17th European Conference, Tel Aviv, Israel, October 23–27, 2022, Proceedings, Part III*. Springer, 576–592. [2](#)
- [13] Peter Hedman, Julien Philip, True Price, Jan-Michael Frahm, George Drettakis, and Gabriel Brostow. 2018. Deep blending for free-viewpoint image-based rendering. *ACM Transactions on Graphics (TOG)* 37, 6 (2018), 1–15. [6](#)
- [14] Fei Hou, Jukai Deng, Xuhui Chen, Wencheng Wang, and Ying He. 2023. NeUDF: Learning Unsigned Distance Fields from Multi-view Images for Reconstructing Non-watertight Models. *arXiv preprint arXiv:2303.15368* (2023). [2](#)
- [15] Shahram Izadi, David Kim, Otmar Hilliges, David Molyneaux, Richard Newcombe, Pushmeet Kohli, Jamie Shotton, Steve Hodges, Dustin Freeman, Andrew Davison, et al. 2011. Kinectfusion: real-time 3d reconstruction and interaction using a moving depth camera. In *Proceedings of the 24th annual ACM symposium on User interface software and technology*. 559–568. [2](#)
- [16] Rasmus Jensen, Anders Dahl, George Vogiatzis, Engin Tola, and Henrik Aanæs. 2014. Large scale multi-view stereopsis evaluation. In *Proceedings of the IEEE conference on computer vision and pattern recognition*. 406–413. [5](#), [7](#), [8](#)
- [17] Michael Kazhdan and Hugues Hoppe. 2013. Screened poisson surface reconstruction. *ACM Transactions on Graphics (ToG)* 32, 3 (2013), 1–13. [1](#), [2](#)
- [18] Diederik P Kingma and Jimmy Ba. 2014. Adam: A method for stochastic optimization. *arXiv preprint arXiv:1412.6980* (2014). [5](#)
- [19] Georgios Kopanas, Julien Philip, Thomas Leimkühler, and George Drettakis. 2021. Point-Based Neural Rendering with Per-View Optimization. In *Computer Graphics Forum*, Vol. 40. Wiley Online Library, 29–43. [6](#)
- [20] Zhaoshuo Li, Thomas Müller, Alex Evans, Russell H Taylor, Mathias Unberath, Ming-Yu Liu, and Chen-Hsuan Lin. 2023. Neuralangelo: High-Fidelity Neural Surface Reconstruction. In *Proceedings of the IEEE/CVF Conference on Computer Vision and Pattern Recognition*. 8456–8465. [1](#), [3](#), [5](#), [7](#), [8](#)
- [21] Xiaoxiao Long, Cheng Lin, Lingjie Liu, Yuan Liu, Peng Wang, Christian Theobalt, Taku Komura, and Wenping Wang. 2022. NeuralUDF: Learning Unsigned Distance Fields for Multi-view Reconstruction

- of Surfaces with Arbitrary Topologies. *arXiv preprint arXiv:2211.14173* (2022). 2, 3
- [22] Xiaoxiao Long, Cheng Lin, Peng Wang, Taku Komura, and Wenping Wang. 2022. Sparseneus: Fast generalizable neural surface reconstruction from sparse views. In *Computer Vision—ECCV 2022: 17th European Conference, Tel Aviv, Israel, October 23–27, 2022, Proceedings, Part XXXII*. Springer, 210–227. 2
- [23] William E Lorensen and Harvey E Cline. 1987. Marching cubes: A high resolution 3D surface construction algorithm. *ACM siggraph computer graphics* 21, 4 (1987), 163–169. 2
- [24] Xiaoxu Meng, Weikai Chen, and Bo Yang. 2023. NeAT: Learning Neural Implicit Surfaces with Arbitrary Topologies from Multi-view Images. In *Proceedings of the IEEE/CVF Conference on Computer Vision and Pattern Recognition*. 248–258. 2
- [25] Ben Mildenhall, Pratul P Srinivasan, Matthew Tancik, Jonathan T Barron, Ravi Ramamoorthi, and Ren Ng. 2021. Nerf: Representing scenes as neural radiance fields for view synthesis. *Commun. ACM* 65, 1 (2021), 99–106. 1, 2, 3, 5, 6, 7, 8
- [26] Thomas Müller, Alex Evans, Christoph Schied, and Alexander Keller. 2022. Instant neural graphics primitives with a multiresolution hash encoding. *ACM Transactions on Graphics (ToG)* 41, 4 (2022), 1–15. 1, 2, 3, 8
- [27] Helen Oleynikova, Alexander Millane, Zachary Taylor, Enric Galceran, Juan Nieto, and Roland Siegwart. 2016. Signed distance fields: A natural representation for both mapping and planning. In *RSS 2016 Workshop: Geometry and Beyond-Representations, Physics, and Scene Understanding for Robotics*. University of Michigan. 2
- [28] Albert Pumarola, Enric Corona, Gerard Pons-Moll, and Francesc Moreno-Noguer. 2021. D-nerf: Neural radiance fields for dynamic scenes. In *Proceedings of the IEEE/CVF Conference on Computer Vision and Pattern Recognition*. 10318–10327. 1, 2
- [29] Paul-Edouard Sarlin, Cesar Cadena, Roland Siegwart, and Marcin Dymczyk. 2019. From Coarse to Fine: Robust Hierarchical Localization at Large Scale. In *CVPR*. 2
- [30] Johannes Lutz Schönberger and Jan-Michael Frahm. 2016. Structure-from-Motion Revisited. In *Conference on Computer Vision and Pattern Recognition (CVPR)*. 2
- [31] Johannes Lutz Schönberger, Enliang Zheng, Marc Pollefeys, and Jan-Michael Frahm. 2016. Pixelwise View Selection for Unstructured Multi-View Stereo. In *European Conference on Computer Vision (ECCV)*. 2, 8
- [32] Rakesh Shrestha, Zhiwen Fan, Qingkun Su, Zuozhuo Dai, Siyu Zhu, and Ping Tan. 2021. Meshmvs: Multi-view stereo guided mesh reconstruction. In *2021 International Conference on 3D Vision (3DV)*. IEEE, 1290–1300. 2
- [33] Jiaxiang Tang, Hang Zhou, Xiaokang Chen, Tianshu Hu, Errui Ding, Jingdong Wang, and Gang Zeng. 2023. Delicate textured mesh recovery from nerf via adaptive surface refinement. *arXiv preprint arXiv:2303.02091* (2023). 6
- [34] Peng Wang, Lingjie Liu, Yuan Liu, Christian Theobalt, Taku Komura, and Wenping Wang. 2021. Neus: Learning neural implicit surfaces by volume rendering for multi-view reconstruction. *arXiv preprint arXiv:2106.10689* (2021). 1, 2, 3, 4, 7, 8
- [35] Yiming Wang, Qin Han, Marc Habermann, Kostas Daniilidis, Christian Theobalt, and Lingjie Liu. 2022. NeuS2: Fast Learning of Neural Implicit Surfaces for Multi-view Reconstruction. *arXiv preprint arXiv:2212.05231* (2022). 2, 3, 5, 7, 8
- [36] Yiqun Wang, Ivan Skorokhodov, and Peter Wonka. 2022. Hf-neus: Improved surface reconstruction using high-frequency details. *Advances in Neural Information Processing Systems* 35 (2022), 1966–1978. 1, 2, 3, 4, 5, 6, 7, 8
- [37] Zhou Wang, Alan C Bovik, Hamid R Sheikh, and Eero P Simoncelli. 2004. Image quality assessment: from error visibility to structural similarity. *IEEE transactions on image processing* 13, 4 (2004), 600–612. 6
- [38] Lior Yariv, Jiatao Gu, Yoni Kasten, and Yaron Lipman. 2021. Volume rendering of neural implicit surfaces. *Advances in Neural Information Processing Systems* 34 (2021), 4805–4815. 2, 7, 8
- [39] Lior Yariv, Yoni Kasten, Dror Moran, Meirav Galun, Matan Atzmon, Basri Ronen, and Yaron Lipman. 2020. Multiview neural surface reconstruction by disentangling geometry and appearance. *Advances in Neural Information Processing Systems* 33 (2020), 2492–2502. 8
- [40] Jingyang Zhang, Yao Yao, Shiwei Li, Tian Fang, David McKinnon, Yanghai Tsin, and Long Quan. 2022. Critical regularizations for neural surface reconstruction in the wild. In *Proceedings of the IEEE/CVF Conference on Computer Vision and Pattern Recognition*. 6270–6279. 8
- [41] Jingyang Zhang, Yao Yao, and Long Quan. 2021. Learning signed distance field for multi-view surface reconstruction. In *Proceedings of the IEEE/CVF International Conference on Computer Vision*. 6525–6534. 2, 8
- [42] Kai Zhang, Gernot Riegler, Noah Snively, and Vladlen Koltun. 2020. Nerf++: Analyzing and

improving neural radiance fields. *arXiv preprint arXiv:2010.07492* (2020). [2](#), [6](#)

- [43] Fuqiang Zhao, Yuheng Jiang, Kaixin Yao, Jiakai Zhang, Liao Wang, Haizhao Dai, Yuhui Zhong, Yingliang Zhang, Minye Wu, Lan Xu, et al. 2022. Human Performance Modeling and Rendering via Neural Animated Mesh. *ACM Transactions on Graphics (TOG)* 41, 6 (2022), 1–17. [1](#), [2](#), [3](#), [4](#), [7](#)
- [44] Heming Zhu, Yu Cao, Hang Jin, Weikai Chen, Dong Du, Zhangye Wang, Shuguang Cui, and Xiaoguang Han. 2020. Deep fashion3d: A dataset and benchmark for 3d garment reconstruction from single images. In *Computer Vision–ECCV 2020: 16th European Conference, Glasgow, UK, August 23–28, 2020, Proceedings, Part I 16*. Springer, 512–530. [2](#)